scientific reports

Check for updates

OPEN

Novel synthesis of siligraphene/tungstates (g-SiC/AWO) with promoted transportation of photogenerated charge carriers via direct Z-scheme heterojunctions

Maryam Afsharpour✉ & Somayeh Darvishi-Farash

We developed here the efficient photocatalysts for the removal of high concentrations of tetracycline under visible light by immobilizing the AWO (A = Ag, Bi, Na) nanocrystals on the surface of siligraphene (g-SiC) nanosheets. The g-SiC/AWO composites was synthesized by magnesiothermic synthesis of g-SiC and sonochemical immobilization of tungstates. These new heterojunctions of g-SiC/tungstates show superior photocatalytic activities in the degradation of high concentrations of tetracycline and 97, 98, and 94% of tetracycline were removed by using low amounts of g-SiC/Ag_2WO_4, g-SiC/Bi_2WO_6, and g-SiC/Na_2WO_4 catalysts, respectively. Based on band structures, the band gaps reduce and the photocatalytic activities were extremely enhanced due to the shortening of electron transfer distance through the Z-scheme mechanism. Also, the graphenic structure of g-SiC is another parameter that was effective in improving photocatalytic performance by increasing the electron transfer and decreasing the rate of electron–hole recombination. Furthermore, the π back-bonding of g-SiC with metal atoms increases the electron–hole separation to enhance the photocatalytic activity. Interestingly, g-SiC composites (g-SiC/AWO) showed much higher photocatalytic properties compared to graphene composites (gr/AWO) and can remove the tetracycline even at dark by producing the oxygenated radicals via adsorption of oxygen on the positive charge of Si atoms in siligraphene structure.

Today, with the progress of human civilization and population growth, we are facing a severe water shortage and reduction of water quality due to various pollutions[1,2]. Wastewaters treatments are very expensive, and traditional methods in addition to imposing heavy costs do not meet the relevant standards in many cases. Recently, with the introduction of new technologies, new solutions such as novel photocatalysts, membranes, and environmentally friendly adsorbents have been introduced for wastewater treatments[3–6]. Photocatalysts are an important class of nanomaterials used in the purification of heavily polluted water and are very effective when other purification methods are not useful or economical[7–10].

Among the wide range of metal-containing photocatalysts[7–17], the tungstates with the general formula of A_2WO_x (AWOs) are considered to be the promising candidates with great photocatalytic potentials due to the unique electronic structure, wide band gap, good chemical stability, and physicochemical properties[18–28]. However, the high recombination rate of photogenerated electron–hole pairs reduces the potential of these catalysts to remove the high concentration pollutants[18–28]. To overcome this limitation, these photocatalysts combined with other materials to reduce the recombination rate. Graphene and its derivations are wildly used as metal-free co-catalysts to enhance photocatalytic performance by promoting charge transfer and reducing the rate of electron–hole recombination[24–31].

Also, interface engineering such as the fabrication of heterojunctions is an effective solution to improve the photogenerated charge separation in photocatalysts. In addition to 2D metal-containing semiconductors such

Department of Inorganic Chemistry, Chemistry and Chemical Engineering Research Center of Iran, Tehran 14335-186, Iran. ✉email: afsharpour@ccerci.ac.ir

as MXenes[32], metal-free semiconductors such as g-C_3N_4 and g-SiC are also considered to be the most promising material for the construction of composite heterojunctions[7,33–39].

Siligraphenes (g-SiCs) are the class of graphenic materials in which a large number of carbon atoms have been replaced by silicon[40–42]. The g-SiC has high thermal, mechanical, and chemical stability along with high surface area, low band gap, and high electron mobility which made it a superior catalyst for removing different organic pollutants at high concentrations[42–47]. The 2D layered structure of siligraphene made it superior candidate to form the well-defined composite heterojunctions. Siligraphene can prevent the aggregation of composites as well as improve the separation of photogenerated electron – hole pairs due to the superior electron mobility of siligraphene. Also, the doping of Si atoms in this structure gives extraordinary properties to this compound compared to graphene, which can make this material a very good candidate for making improved catalysts with graphenic structures. So far none has reported the potential of siligraphene coupled with tungstates (AWOs) for removal of organic pollutants in water.

In this work, the new Z-scheme heterojunctions of Ag_2WO_4, Bi_2WO_6, and Na_2WO_4 with siligraphene (g-SiC) were synthesized for removal of high concentration of tetracycline under visible light. Siligraphene (g-SiC) was synthesized via a low-temperature method to maintain the porous structure and g-SiC/AWO composites were developed by immobilizing of tungstates on the surface of g-SiC. Siligraphene can decrease the band gap, increase the charge transfer, and decrease the rate of photogenerated electron–hole recombination.

Result and discussion

Characterization of g-SiC/Ag_2WO_4, g-SiC/Bi_2WO_6, and g-SiC/Na_2WO_4. Figure 1 shows the FT-IR spectra of g-SiC catalysts. FT-IR spectra of g-SiC shows the Si–C stretching vibration at 813 cm^{-1} which confirms the formation of a bond between silicon and carbon. The g-SiC/Ag_2WO_4 spectra shows the stretching vibration of the Si–C bond at 785 cm^{-1} which is shifted to a lower frequency compared to g-SiC (813 cm^{-1}), indicating the stronger Si–C bond. The stretching vibrations of the W–O bond appeared at 823 cm^{-1} and the bands at 570–650 cm^{-1} are related to W–O–W and O–W–O asymmetric stretching vibrations of the WO_4^{2-} anion[48].

The Si–C stretching vibration was observed at 816 cm^{-1} in g-SiC/Bi_2WO_6 catalyst which is slightly shifted to a higher frequency compared to g-SiC which indicates the immobilization of Bi_2WO_6 on the surface of g-SiC. The absorption bands that appeared at 582 and 470 cm^{-1} are related to Bi–O vibrations, and the absorption bands in the region of 729 cm^{-1} is corresponds to W–O vibration[49].

The absorption band of Si–C appeared at 837 cm^{-1} in g-SiC/Na_2WO_4 catalyst. The W–O vibration of WO_4^{-2} anion is observed in the 810 cm^{-1} and the band at 472 cm^{-1} is related to W–O–W vibration[50].

Figure 2 shows the XRD diffraction pattern of g-SiC/Ag_2WO_4, g-SiC/Bi_2WO_6, and g-SiC/Na_2WO_4 compared to g-SiC. The Ag_2WO_4 diffraction peaks were observed at 2Θ of 16.65, 29.95, 30.95, 33.15, 44.55, 46.15, 53.7, 55.6, 56.75, 65.01, and 77.9° in g-SiC/Ag_2WO_4 which represent the mixture of α and β phases of Ag_2WO_4 (JCPDS #34-0061; orthorhombic α- Ag_2WO_4) and (JCPDS #33-1195; hexagonal β- Ag_2WO_4)[19,48].

In the g-SiC/Bi_2WO_6 sample, the diffraction peaks observed at 2Θ of 28.35, 32.95, 47.20, 56.16, 58.77, 76.06, and 78.61° indicate the (131), (200), (202), (310), (226), (113), and (139) planes of the orthorhombic structure of Bi_2WO_6 (JCPDS #39-0256)[49].

Figure 2 shows that in g-SiC/Na_2WO_4 sample, the diffraction peaks of sodium tungstate were observed at 16.95, 27.75, 32.65, 43.40, 48.95, 52.05, 57.05, 59.95, 64.75, 67.45, 74.35, and 78.30° which indicate the (111), (220), (311), (331), (422), (511), (440), (620), (533), (444), and (642) planes (JCPDS# 12-772)[51].

In all samples, the weak diffraction peaks of the hexagonal 6H-SiC structure were observed which indicates the covering of g-SiC surface with tungstate particles. 6H-SiC is a hexagonal polytype of SiC with stacking

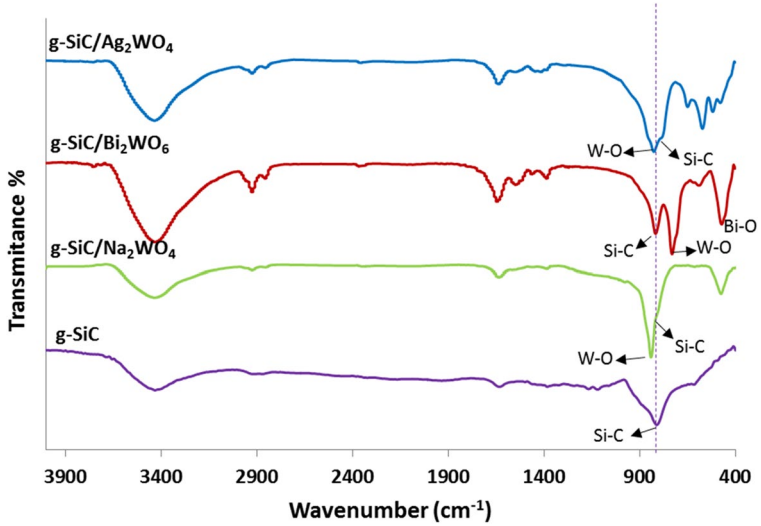

Figure 1. FT-IR spectra of g-SiC, g-SiC/Ag_2WO_4, g-SiC/Bi_2WO_6, and g-SiC/Na_2WO_4.

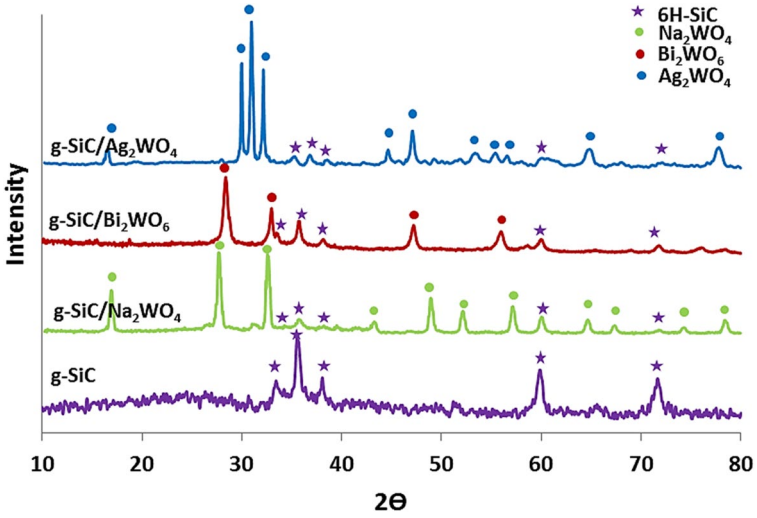

Figure 2. XRD diffraction patterns of g-SiC, g-SiC/Ag_2WO_4, g-SiC/Bi_2WO_6, and g-SiC/Na_2WO_4.

sequence repeats every six bilayers along the c-axis direction. The diffraction peaks of the g-SiC were observed at 31.61, 35.58, 37.98, 60.08, and 71.76 representing the (101), (102), (103), (110), and (202) planes in the hexagonal structure of g-SiC (JCPDS#-29-1128)[42–47]. The high amounts of immobilized tungstates (AWO) on the surface of g-SiC have led to the observation of weak diffractions from 6H-SiC in these composites.

The lattice fringe data were recorded in Table S1.

Figure 3 shows the SEM images of synthesized catalysts. As shown in Fig. 3, needle-like, nanoparticle, and plate-like morphologies of Ag_2WO_4, Bi_2WO_6, and Na_2WO_4 were observed on the surface of g-SiC in g-SiC/Ag_2WO_4, g-SiC/Bi_2WO_6, and g-SiC/Na_2WO_4 catalysts, respectively.

Figure 4a displays the N_2 adsorption/desorption isotherms of g-SiC, g-SiC/Ag_2WO_4, g-SiC/Bi_2WO_6, and g-SiC/Na_2WO_4, which shows the decrease of surface area after immobilization of AWO on the surface of g-SiC. These results can be justified by the filling of pores in g-SiC by AWO particles, which is shown in pore size distribution curves (Fig. 4b). In g-SiC/Na_2WO_4, different pore distribution and higher surface area was observed, indicating the formation of new porosity of surface due to the larger size of Na_2WO_4 particles (Fig. 4b and Fig. 3c).

Figure 5a illustrates the band gaps of synthesized catalysts based on UV–Vis drift reflectance spectra. As can be seen, the band gaps of g-SiC/Ag_2WO_4, g-SiC/Bi_2WO_6, and g-SiC/Na_2WO_4 are calculated as 2.83, 2.80, and 2.88 eV, respectively (Fig. 5). Results show the decreases of band gap of tungstate compounds after stabilization on the surface of g-SiC. The band gap of Ag_2WO_4, Bi_2WO_6, and Na_2WO_4 are reported 3.1, 2.89, and 3.7 eV, respectively[26,50,52] which decrease after forming a heterojunction with g-SiC (band gap = 1.99 eV).

Photoluminescence (PL) spectra of synthesized samples were shown in Fig. 5b to evaluate the degree of charge recombination[53]. As shown in Fig. 5b, the PL intensities of g-SiC/AWO samples decrease significantly in

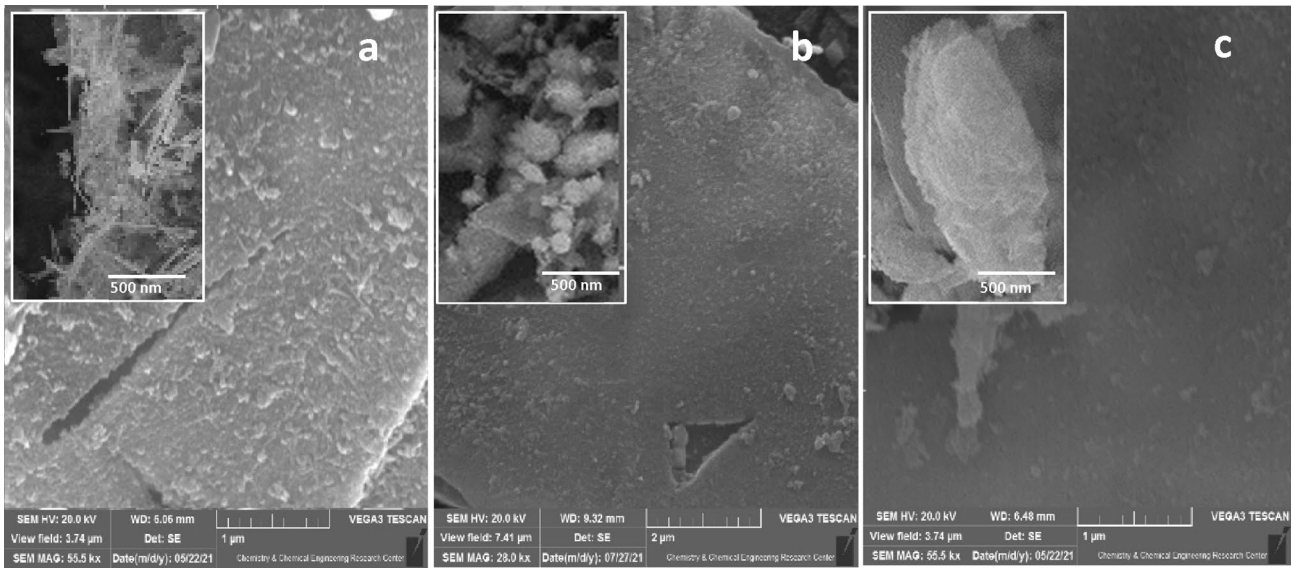

Figure 3. SEM images of g-SiC/Ag_2WO_4 (**a**), g-SiC/Bi_2WO_6 (**b**), and g-SiC/Na_2WO_4 (**c**).

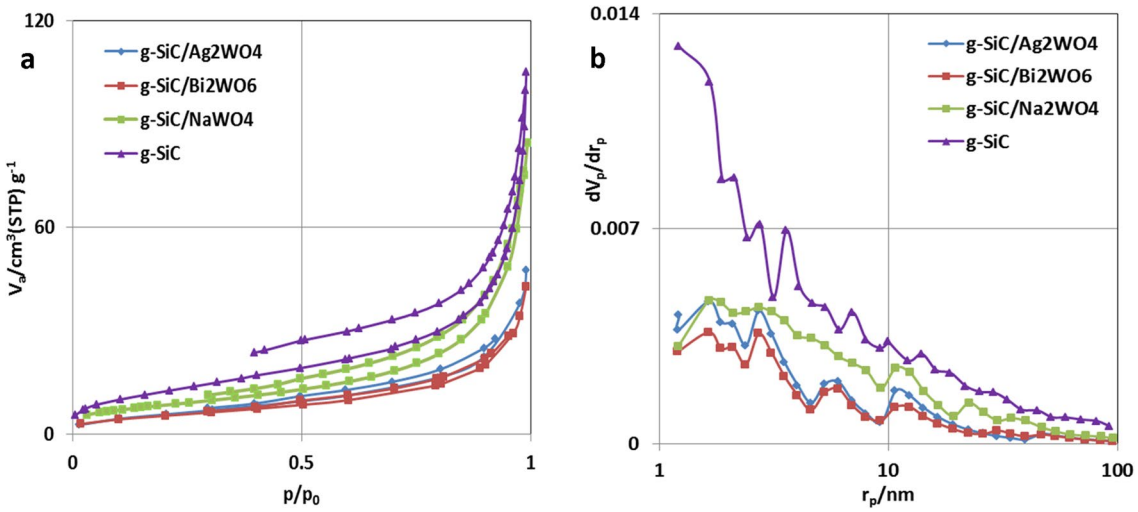

Figure 4. N_2 adsorption/desorption isotherms and pore size distribution curves of g-SiC, g-SiC/Ag_2WO_4, g-SiC/Bi_2WO_6, and g-SiC/Na_2WO_4.

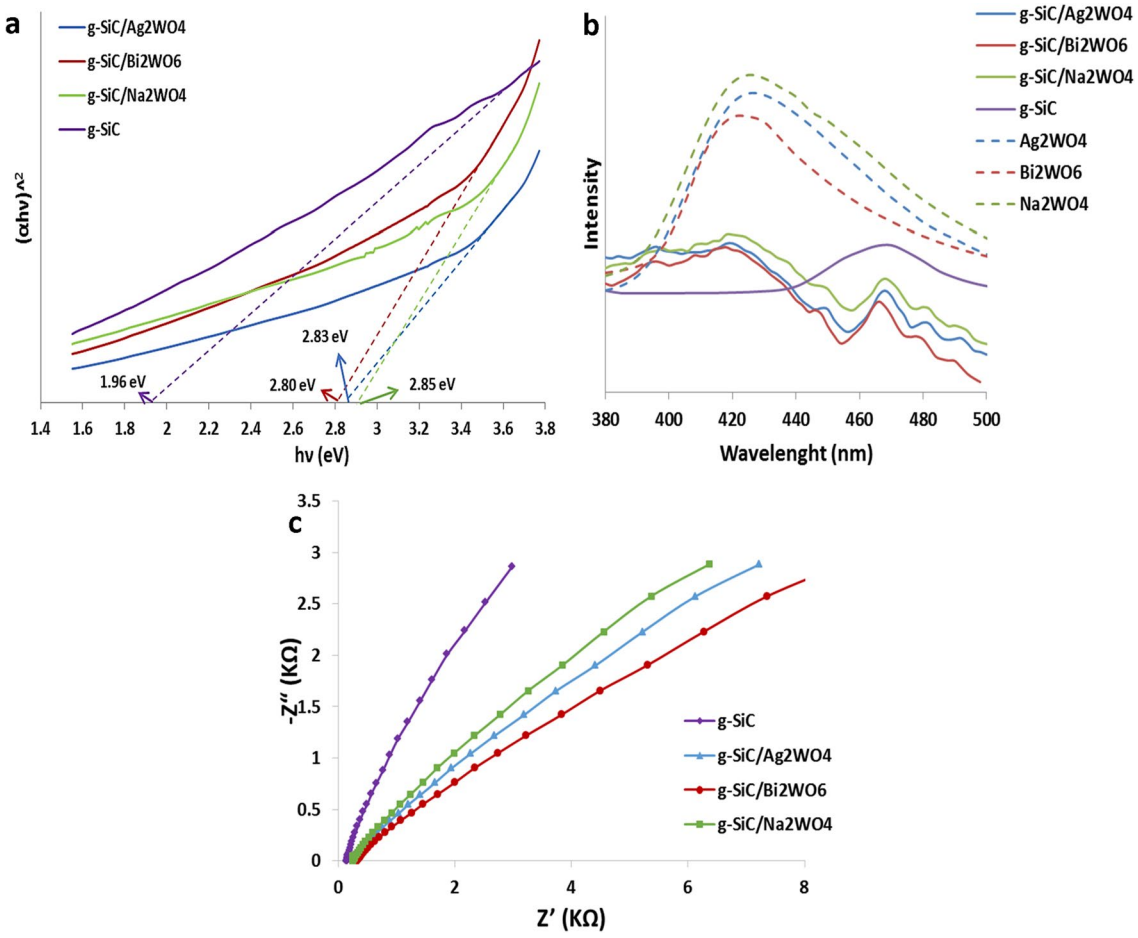

Figure 5. Band gap (**a**), photoluminescence (PL) spectra (**b**), and Nyquist plots (EIS) (**c**) of g-SiC, g-SiC/Ag_2WO_4, g-SiC/Bi_2WO_6, and g-SiC/Na_2WO_4.

comparison with the pure Ag_2WO_4, Bi_2WO_6, and Na_2WO_4, which indicates that the immobilization of tungstates on the g-SiC surface decrease the recombination rate of photogenerated electron-holes. In g-SiC/AWO samples, photogenerated electrons could be transferred efficiently from tungstates to g-SiC due to the high charge carrier of the g-SiC sheets.

The efficiency of photogenerated electron–hole separation of synthesized samples was further studied by the electrochemical impedance spectroscopy (EIS)[54]. As shown in Fig. 5c, the Nyquist plots of the g-SiC/AWO samples exhibit the smaller resistance than g-SiC, indicating the better separation efficiency of photogenerated charge carriers and therefore enhanced photocatalytic activities.

Photocatalytic results

The photocatalytic performance of g-SiC, g-SiC/Ag_2WO_4, g-SiC/Bi_2WO_6, and g-SiC/Na_2WO_4 in comparison with Ag_2WO_4, Bi_2WO_6, and Na_2WO_4 and their graphene composites (gr/AWO) were reported in Fig. 6. As can be seen, immobilization of tungstate catalysts on the surface of g-SiC enhances the photocatalytic degradation of TCL and 97, 98, and 94% removal of TCL (50 ppm) were observed for g-SiC/Ag_2WO_4, g-SiC/Bi_2WO_6, and g-SiC/Na_2WO_4 after 20 min, respectively (Fig. 6). While, Ag_2WO_4, Bi_2WO_6, and Na_2WO_4 show the weak photocatalytic performances in the removal of high concentrations tetracycline (50 ppm), and 16, 25, and 18% TCL removal were observed after 100 min (Fig. 6). These results show the good effect of g-SiC as catalyst support. Figure 6 also shows that g-SiC as a metal-free catalyst represents better photocatalytic activity than tungstate catalysts and can remove 80% of TCL in a shorter time (30 min). This shows that g-SiC does not only play the role of catalyst support and acts as a photocatalyst to create a heterojunction with tungstates, which can improve the catalytic performances of tungstate photocatalysts (Fig. 6).

To better understand the effect of g-SiC on the photocatalytic performance of g-SiC/AWO composites, the photocatalytic properties of immobilized Ag_2WO_4, Bi_2WO_6, and Na_2WO_4 on the surface of graphene (gr/AWO) were also compared with g-SiC/AWO composites (Fig. 6). As we know, graphene along with other semiconductors like tungstates can improve the photocatalytic properties by increasing the transfer of electron and decreasing the rate of electron–hole recombination[24–28]. Therefore, better photocatalytic activities can be seen in gr/AWO composites than in tungstates alone (Fig. 6).

As seen in Fig. 6, replacing siligraphene (g-SiC) instead of graphene (gr) shows significant increases in photocatalytic properties. The g-SiC is a graphene structure in which half of its C atoms have been replaced by Si atoms. This graphene structure can increase the catalytic activity due to its high electron mobility. Besides charge transfer capability, also photogenerated charge lifetime contributes to the photocatalytic reaction. Interactions between g-SiC and Ag_2WO_4, Bi_2WO_6, or Na_2WO_4 can reduce the rate of electron–hole recombination and improve photocatalytic performance. Also, π electrons in the siligraphene structure can form the π back-bonding with metal atoms and increase the electron–hole separation and enhance the photocatalytic activity[55].

In addition to the advantages of graphene structure in g-SiC composites, the heterojunctions created with g-SiC reduce the band gap and can enhance the photocatalytic activity by shortening the electron transfer distance through the Z-scheme mechanism which will be explained later in this discussion.

Another mechanism that plays a role in enhancing the catalytic properties of g-SiC composites (g-SiC/AWO) is related to the surface charges in the g-SiC structure. According to our previous report, due to the electronegativity difference between Si and C in the g-SiC (siligraphene) structure, Si atoms have a partial positive charge and C atoms have a partial negative charge[7,10,42]. The dissolved O_2 in a solution can adsorb on positive charged Si atoms in g-SiC, the O–O bonds dissociated and the oxygenated radicals were formed that can proceed the photocatalytic oxidation process[7,10,42]. As shown in Fig. 6, 64–85% TCL removal were observed at the time zero for g-SiC composites (g-SiC/AWO), indicating the degradation of TCL even at dark via oxidation of TCL by

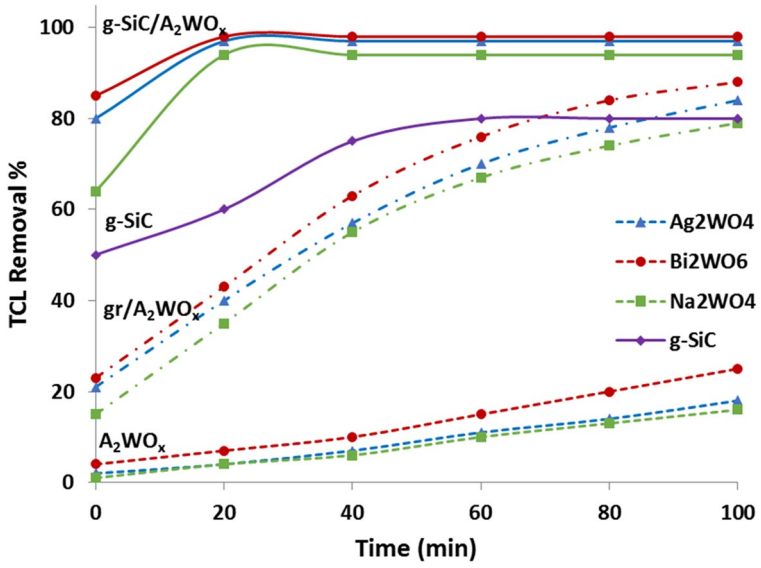

Figure 6. Comparison of photocatalytic performances of AWO, gr/AWO, g-SiC, and g-SiC/AWO composites in removal of 50 ppm TCL.

formed oxygenated radicals. While, in the graphene composites (gr/AWO), only 15–23% TCL removal was observed at dark due to the adsorption of TCL on the surface of graphene (Fig. 6).

As shown in Fig. 4, the BET results confirm the reduction of surface area in g-SiC/AWO composites. These data show that the increases in catalytic properties are related to the structural properties of immobilized tungstates on the surface of g-SiC, and the effect of the chemical structure was dominant over the effect of the surface area.

To achieve the best results, the reaction conditions were optimized in Fig. 7. Figure 7a–c represents the photocatalytic results in the removal of different concentrations of TCL. As can be seen, with the increase in TCL concentration, the removal has decreased. An increase in TCL concentration causes the saturation of the photocatalyst surface which decreases the photocatalytic activity.

The effect of catalyst amounts was also investigated by using g-SiC/Bi_2WO_6 as the best photocatalyst (Fig. 7d). Results show that increasing the amounts of photocatalyst from 0.01 to 0.015 g increases the catalytic performance. Increasing the amount of catalyst to 0.02 g only increases the rate of degradation (Fig. 7d).

The effect of pH in photocatalytic removal of TCL by g-SiC, g-SiC/Ag_2WO_4, g-SiC/Bi_2WO_6, and g-SiC/Na_2WO_4 catalysts were shown in Fig. 7e. As TCL has the several functional groups, different ionized species were

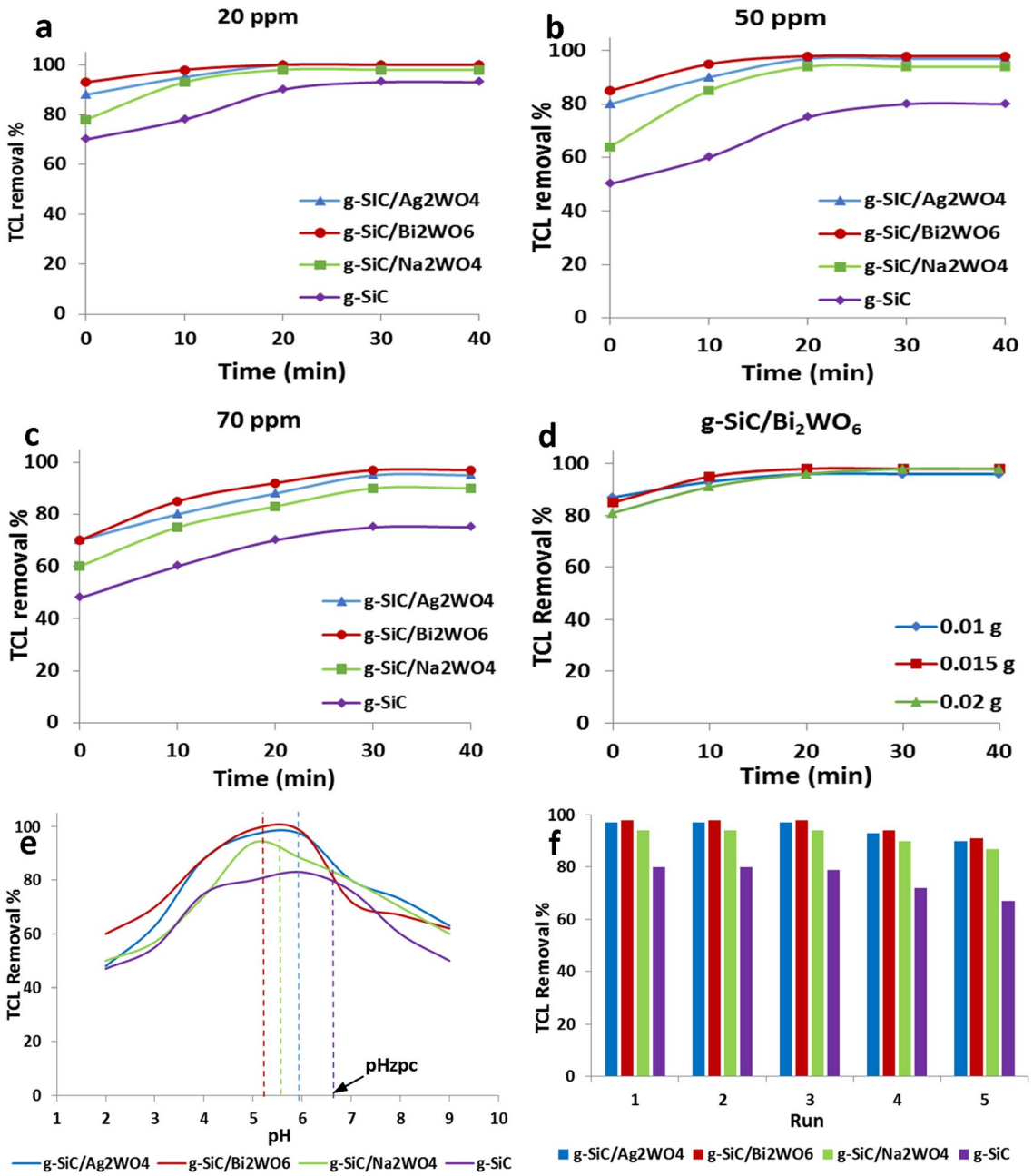

Figure 7. Photocatalytic removal of 20 ppm (**a**), 50 ppm (**b**), and 70 ppm (**c**) TCL in Visible light, different amounts of g-SiC/Bi_2WO_6 catalyst (**d**), effect of pH (**e**), and recovery of catalysts (**f**).

formed at different pH. The H_2TC^+ species was observed at pH < 3.3, H_2TC^0 zwitterionic species was formed at pH 3.3–7.7, and HTC^-/TC^{2-} species was produced at pH > 7.7[56,57]. As known, the surface charge of the catalyst becomes positive at a pH lower than pH_{zpc}, which can absorb the negative molecules. The pH_{zpc} of g-SiC, g-SiC/Ag_2WO_4, g-SiC/Bi_2WO_6, and g-SiC/Na_2WO_4 were measured 6.7, 5.9, 5.2, and 5.6, respectively. So, at pH_{zpc} of catalysts (pH = 5–7), H_2TC^0 as the main species of TCL can be adsorbed on the surface of catalysts via interaction of negative tricarbonyl amide groups of TCL with a positive charge of Si atoms on the g-SiC structure[10]. At a pH lower than 3.3, the TCL removal decreases due to the repulsion between the H_2TC^+ species of TCL and the positive surface of catalysts. Also, at a pH higher than 7.7, the photocatalytic performances were decreased which is related to electrostatic repulsion between the negative surface of catalysts and HTC^-/TC^{2-} species of TCL (Fig. 7e).

To check the stability of the catalysts, their recovery was also investigated. As can be seen in Fig. 7f, no change in the photocatalytic efficiency can be observed after 3 runs. In the next runs, a slight drop in the photocatalytic activity is seen, which is related to the saturation of the catalyst surfaces. The g-SiC catalyst has a lower photocatalytic ability, so a greater drop in recovery is observed. A lower drop in the activity of tungstate catalysts (g-SiC/AWO) indicates the high activity of these photocatalysts in the continuous recovery.

Figure 8 shows the proposed mechanism of photocatalytic degradation by g-SiC/Ag_2WO_4, g-SiC/Bi_2WO_6, and g-SiC/Na_2WO_4 composites. Based on band structures, these semiconductors are excited under visible light irradiation and electrons and holes are created in the valence (VB) and conduction (CB) bonds. The CB and VB potentials of g-SiC/AWO catalysts were predicted by the following equation:

$$E_{VB} = X - E_e + 0.5\,E_g$$

$$E_{CB} = E_{VB} - E_g$$

X is the electronegativity of the semiconductor and E_e is the energy of free electrons in the hydrogen scale (approximately 4.5 eV). The *X* value of g-SiC/Ag_2WO_4, g-SiC/Bi_2WO_6, and g-SiC/Na_2WO_4 are reported 6, 6.36, and 6.5 eV, respectively[48,50,58]. The E_g of Ag_2WO_4, Bi_2WO_6, and Na_2WO_4 were measured from UV–Vis spectra 3.1, 2.89, and 3.7 eV, respectively (Fig. 5b). As a result, E_{CB} and E_{VB} for Ag_2WO_4, Bi_2WO_6, and Na_2WO_4 have been calculated as − 0.05 and 3.05 eV, 0.41 and 3.30 eV, and 0.15 and 3.85 eV, respectively. The E_g of g-SiC was obtained at 1.99 eV from UV–Vis spectra (Fig. 5b) and E_{VB} was measured at 1.24 eV from XPS spectra (Fig. S1). As a result, the E_{CB} of g-SiC has been calculated as − 0.72 eV. Based on energy levels of g-SiC and its tungstate catalysts, the CB of g-SiC (− 0.72 V) is more negative than $O_2/\cdot O_2^-$ (− 0.33 V) and the VB of Ag_2WO_4 (3.05 V), Bi_2WO_6 (3.3 V), and Na_2WO_4 (3.85 V) are more positive than $OH^-/\cdot OH$ (+ 1.99 V), so, the photogenerated e^- can reduce the O_2 to form $\cdot O_2^-$ radicals and photogenerated h^+ can oxidize OH^- to produce ·OH radicals. Results confirm the electrons in the CB of AWO combine directly with the holes in the VB of g-SiC, indicating the direct Z-scheme mechanism in the charge transfer path of photogenerated electron–hole in g-SiC/AWO heterojunctions.

Traditional BWO-based heterojunction is commonly performed via the Type-II strategy to accelerate the rate of charge transfer. These conventional heterojunction has a drawback that charge migration causes the photogenerated electron–hole to have weak redox ability[59–61]. In this novel Z-scheme heterojunction not only gives photocatalyst with superior redox ability, but also accelerates the migration of photogenerated electron-holes[62].

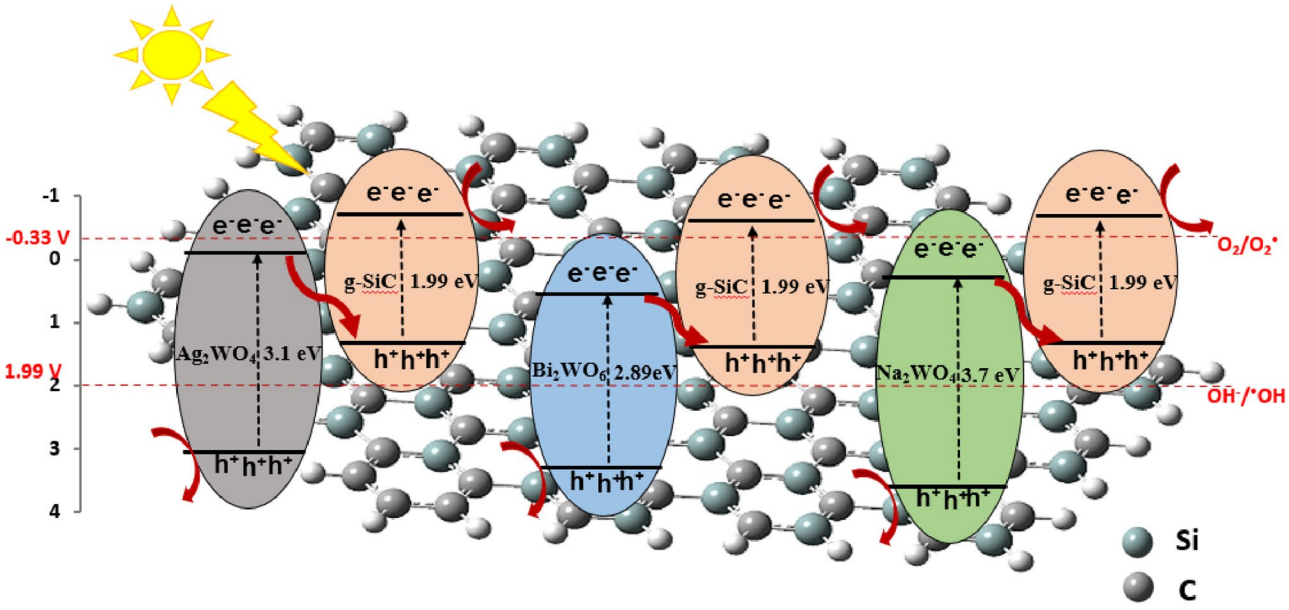

Figure 8. Z-Scheme mechanism of photocatalytic degradation by g-SiC/Ag_2WO_4, g-SiC/Bi_2WO_6, and g-SiC/Na_2WO_4 composites.

Figure 8 clearly shows that the heterojunctions created with g-SiC reduce the band gaps and can enhance the photocatalytic properties by shortening the electron transfer distance through the Z-scheme mechanism. The smaller band gap and shorter electron transfer path which enhances the stability of carrier transfer in Bi_2WO_6 is the reason for the better photocatalytic activity of this catalyst.

The quenching tests were also done to identify the active radicals involved in photocatalytic reaction for g-SiC/AWO catalysts (Fig. 9). The quenching results of g-SiC indicate the involvement of $^{\cdot}OH$ and $^{\cdot}O_2^-$ radicals as the main species in the degradation of TCL. While, in g-SiC/AWO photocatalysts, $^{\cdot}OH$ and h^+ are the reactive species in the photocatalytic reaction, and $^{\cdot}O_2^-$ radical shows the lower involvement in the degradation of TCL (Fig. 9).

In general, it can be concluded that by using the g-SiC as catalyst support, new Z-scheme heterojunctions of tungstates (g-SiC/AWO) can be developed to find out the visible light degradation of high concentration of antibiotics by improving the charge separation, enhancing the electron transfer in Z-scheme heterojunction, and decreasing the rate of photogenerated electron–hole recombination.

Methods

Materials and instruments. Perlite (SiO_2: 98%, porosity: 85%) was used as natural precursor of Si source and citric acid as a C source were purchased from Merck. Ethanol (96%), Mg powder (0.3–0.06 µm), hydrochloric acid (37%), and hydrofluoric acid (40%) were obtained from Merck.

FT-IR spectra were obtained from Bruker, Vector instrument. Scanning electron microscopy (SEM) was used to study the morphology of samples by TESCAN, VEGA3 microscope armed with the X-ray energy dispersive spectroscope (EDX), and TEM microscopy was done using Zeiss, EM10C microscope. Crystalline phases were identified by BrukerAxs, D8 Advance X-ray diffractometer (XRD) using CuK_α radiation. Raman spectra were obtained with Bruker, Senterra Raman spectrometer with a 785 nm laser. N_2 adsorption/desorption isotherms and the pore size distributions were recorded by Belsorp mini instrument. XPS analysis was recorded from ESCALAB 250Xi Thermo Scientific system (MgKα = 1253.6 eV).

Synthesis of g-SiC (siligraphene). Citric acid was used as a carbon source and prepared by dissolving 0.8 g of citric acid in 100 mL of distilled water. Perlite powder was first washed with HCl (1 M) solution to remove its impurities and dried at 70 °C for 8 h. Then, 2 g of perlite was added to 200 mL of citric acid (8 g/L) solution and sonicated for 15 min. The powder filtered and dried at oven. To better penetration of citric acid to perlite pores, this process repeated 5 times. Finally, the mixture was dried at 80 °C for 24 h. The obtained powder was put in a furnace at 800 °C (5 °C /min) for 1 h under an N_2 atmosphere to obtain the SiO_2/carbon composite. To form the Si–C bond, the composite was mixed with Mg powder with the Si:Mg ratio of 1:2 and heated at 800 °C for 5.5 h under an N_2 atmosphere (5 °C /min). To eliminate the impurity of MgO, the produced g-SiC was immersed in HCl solution (2 M) for 48 h and then washed with distilled water to remove $MgCl_2$. The residual silica was removed by immersing the produced g-SiC in 2 M HF solution. Afterward, the g-SiC (siligraphene) was filtered and dried in a vacuum oven at 60 °C for 24 h.

Synthesis of g-SiC/AWO (A=Ag, Bi, Na). For stabilization of Ag_2WO_4 and Bi_2WO_6 on g-SiC (siligraphene), 0.2 g of synthesized g-SiC was sonicated for 10 min in a certain amount of distilled water. Silver or bismuth solution was prepared by dissolving 0.1 g of silver or bismuth nitrate in 25 mL of distilled water and stirring for 0.5 h. Then, Ag or Bi solution was added to g-SiC suspension and stirred for 0.5 h. Tungsten solution was also prepared by dissolving 0.1 g of sodium tungstate in 25 mL of distilled water for 0.5 h, then added dropwise to Ag/g-SiC or Bi/g-SiC mixture under sonication. The final mixtures were placed in an oven at 160 °C for 5 h. The solid powder was filtered and dried at 70 °C.

The g-SiC/Na_2WO_4 was also synthesized by adding 0.1 g of sodium tungstate to g-SiC suspension under sonication. The mixture was heated at 160 °C for 5 h. The solid product was filtered and dried at 70 °C.

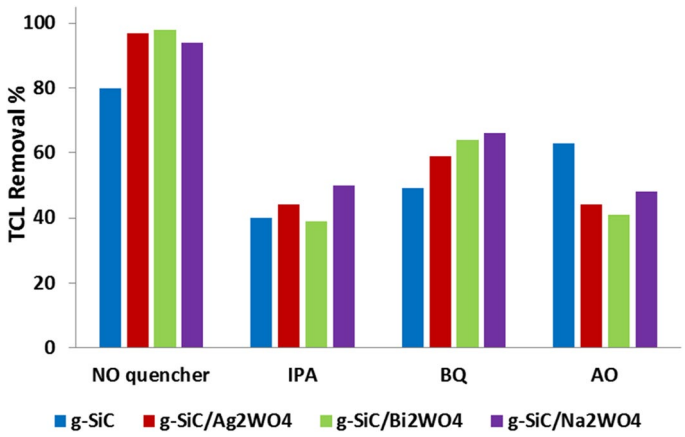

Figure 9. Quenching experiments of photocatalytic removal of TCL (ppm 50).

Photocatalytic experiments. To investigate the photocatalytic performance, the removal of tetracycline (TCL) as a drug pollutant were evaluated. In a batch experiment, a certain amount of g-SiC/Ag_2WO_4, g-SiC/Bi_2WO_6, and g-SiC/Na_2WO_4 photocatalysts was dispersed in 10 mL of tetracycline (TCL) solution under stirring. The solution saturates with oxygen by air bubbling into the system and irradiated by visible light. To optimize the photocatalytic reaction, different concentrations of TCL (20, 50, and 70 ppm) were tested by using 0.01, 0.015, and 2 g of catalyst at pH of 2–12. Before irradiation, all samples were stirred at dark for 5 min, and then the photocatalytic process was performed. The concentration of dye in the solution was measured by UV–Vis spectroscopy after each 20 min. After each 10 min, the concentration of TCL was measured by UV–Vis spectroscopy at 357 nm. The TCL removal percent was determined using the following equation:

$$\text{Removal } \% \ = \left[\frac{(C_0 - C_t)}{C_0}\right] * 100\%$$

where C_0 and C_t are the initial and equilibrium TCL concentrations.

Quenching experiments were done by using 2 Mm of isopropanol (IPA) as hydroxyl radical ($^{\cdot}OH$) scavenger, 1,4-benzoquinone (BQ) as superoxide radical anions ($^{\cdot}O_2^-$) scavenger, and ammonium oxalate (AO) as the scavenger of the hole (h^+).

Conclusion

The new Z-scheme heterojunctions of siligraphene (g-SiC) with different tungstates (Ag_2WO_4, Bi_2WO_6, and Na_2WO_4) were synthesized and their photocatalytic properties were investigated in the removal of tetracycline. Based on the photocatalytic degradation results, the photocatalytic potentials of tungstates catalysts were promoted by immobilizing on the surface of g-SiC. The graphenic structure of g-SiC can improve photocatalytic performance by increasing the electron transfer and decreasing the rate of electron–hole recombination. Also, the π back-bonding of g-SiC with metal atoms increases the electron–hole separation to enhance the photocatalytic activity. Furthermore, the heterojunctions created with g-SiC reduce the band gap and can enhance the photocatalytic activity by shortening the electron transfer distance through the Z-scheme mechanism. The optimized g-SiC/AWO composites exhibited high photocatalytic performances and 97, 98, and 94% of high concentrations tetracycline (50 ppm) were removed after 20 min by using only 10 mg of g-SiC/Ag_2WO_4, g-SiC/Bi_2WO_6, and g-SiC/Na_2WO_4 catalysts, respectively. The g-SiC/Bi_2WO_6 photocatalyst shows the highest photocatalytic activity due to the smaller band gap and shorter electron transfer path.

Data availability

All data generated or analyzed during this study are included in this published article.

Received: 3 March 2023; Accepted: 17 June 2023
Published online: 20 June 2023

References

1. Antil, R. Problems and prospectus of utilization of sewage and industrial wastewaters in agriculture. *Tox. Environ. Chem.* **96**, 1260–1271 (2014).
2. Seckler, D., Barker, R. & Amarasinghe, U. Water scarcity in the twenty-first century. *Intern. J. Water. Res. Develop.* **15**, 29–42 (1999).
3. Cai, Z. *et al.* An overview of nanomaterials applied for removing dyes from wastewater. *Environ. Sci. Pollut. Res.* **24**, 15882–15904 (2017).
4. Muralikrishna, I. V. & Manickam, V. Industrial Wastewater Treatment Technologies, Recycling, and Reuse. In: *Environmental Management*, 295–336 (Elsevier, 2017).
5. Hermosilla, D., Merayo, N., Gascó, A. & Blanco, A. The application of advanced oxidation technologies to the treatment of effluents from pulp and paper industry: A review. *Environ. Sci. Pollut. Res.* **22**, 168–191 (2015).
6. Katheresan, V., Kansedo, J. & Lau, S. Y. Efficiency of various recent wastewater dye removal methods: A review. *J. Environ. Chem. Eng.* **6**, 4676–4697 (2018).
7. Darvishi-Farash, S., Afsharpour, M. & Heidarian, J. Novel siligraphene/g-C_3N_4 composites with enhanced visible light photocatalytic degradations of dyes and drugs. *Environ. Sci. Pollut. Res.* **28**, 5938–5952 (2021).
8. Chen, D. *et al.* Photocatalytic degradation of organic pollutants using TiO_2-based photocatalysts: A review. *J. Clean. Product.* **268**, 121725 (2020).
9. Afsharpour, M., Elyasi, M. & Javadiaan, H. R. A novel N-doped nanoporous bio-graphene synthesized from *Pistacia lentiscus* gum and Its nanocomposite with WO_3 nanoparticles: Visible-light-driven photocatalytic activity. *Molecule* **26**, 6569 (2021).
10. Afsharpour, M., Behtooei, H. R., Shakiba, M. & Martí, V. Novel N, P, S co-doped graphenic SiC layers (g-SiC) in visible-light photodegradation of antibiotics and inactivating the bacteria. *Process Saf. Environ. Protect.* **166**, 704–717 (2022).
11. Wang, X. *et al.* All-solid-state Z-scheme Pt/ZnS-ZnO heterostructure sheets for photocatalytic simultaneous evolution of H_2 and O_2. *Chem. Eng. J.* **385**, 123782 (2020).
12. Lin, Q. *et al.* Hierarchically periodic Macroporous CdS–ZnO heterojunctions with multiple quantum well-like band alignments for efficient photocatalytic hydrogen evolution without a cocatalyst. *ACS Sustain. Chem. Eng.* **11**, 3093–3102 (2023).
13. Vijayakumar, N. *et al.* Synthesis and characterization of calcium and magnesium based oxides and titanates for photocatalytic degradation of rhodamine B: A comparative study. *Sci. Rep.* **13**, 3615 (2023).
14. Khodamorady, M. & Bahrami, K. A novel ZnS-CdS nanocomposite as a visible active photocatalyst for degradation of synthetic and real wastewaters. *Sci. Report.* **13**, 2177 (2023).
15. Bowen, Y. *et al.* Synergy effect between tetracycline and Cr (VI) on combined pollution systems driving biochar-templated Fe_3O_4@SiO_2/TiO_2/g-C_3N_4 composites for enhanced removal of pollutants. *Biochar.* **5**, 1 (2023).
16. Afsharpour, M. & Amoee, S. Porous biomorphic silica@ZnO nanohybrids as the effective photocatalysts under visible light. *Environ. Sci. Pollut. Res.* **29**, 49784–49795 (2022).
17. Chen, L. *et al.* Excellent photocatalysis of Bi_2WO_6 structured with oxygen vacancies in degradation of tetracycline. *J. Mol. Struct.* **1278**, 134911 (2023).
18. Gouveia, A. F. *et al.* Ag_2WO_4 as a multifunctional material: Fundamentals and progress of an extraordinarily versatile semiconductor. *J. Mater. Res. Technol.* **21**, 4023E4051 (2022).

19. Alvarez-Roca, R. *et al.* Selective synthesis of α-, β-, and γ-Ag_2WO_4 polymorphs: Promising platforms for photocatalytic and antibacterial materials. *Inorg. Chem.* **60**, 1062–1079 (2021).
20. Ma, Q. *et al.* Visible light active graphene oxide modified $Ag/Ag_2O/BiPO_4/Bi_2WO_6$ for photocatalytic removal of organic pollutants and bacteria in wastewater. *Chemosphere* **306**, 135512 (2022).
21. Raizada, P. *et al.* Magnetically retrievable Bi_2WO_6/Fe_3O_4 immobilized on graphene sand composite for investigation of photocatalytic mineralization of oxytetracycline and ampicillin. *Process Saf. Environ. Prot.* **106**, 104–116 (2017).
22. Yang, X. *et al.* Graphene dispersed Bi_2WO_6 nanosheets with promoted interfacial charge separation for visible light photocatalysis. *ChemCatChem* **11**, 5487–5494 (2019).
23. Yao, B. *et al.* Effect of surface and internal Bi^0 on the performance of the Bi_2WO_6 photocatalyst. *J. Alloy. Comp.* **935**, 168052 (2023).
24. Mengting, Zh., Kurniawan, T. A., Yanping, Y., Avtar, R. & Othman, M. H. D. 2D Graphene oxide (GO) doped p-n type BiOI/Bi_2WO_6 as a novel composite for photodegradation of bisphenol A (BPA) in aqueous solutions under UV-vis irradiation. *Mater. Sci. Eng. C.* **108**, 110420 (2020).
25. Yang, J., Wang, X., Zhao, X., Dai, J. & Mo, Sh. Synthesis of uniform Bi_2WO_6-reduced graphene oxide nanocomposites with significantly enhanced photocatalytic reduction activity. *J. Phys. Chem. C.* **119**, 3068–3078 (2015).
26. Zhou, Y., Ren, S., Dong, Q., Li, Y. & Ding, H. One-pot preparation of Bi/Bi_2WO_6/reduced graphene 1 oxide as a plasmonic photocatalyst with improved activity under visible light. *RSC Adv.* **49**, 102875–102885 (2016).
27. Sun, S., Wang, W. & Zhang, L. Bi_2WO_6 quantum dots decorated reduced graphene oxide: Improved charge separation and enhanced photoconversion efficiency. *J. Phys. Chem. C.* **117**, 113–9120 (2013).
28. Sun, Zh. *et al.* A high-performance Bi_2WO_6–graphene photocatalyst for visible light-induced H_2 and O_2 generation. *Nanoscale* **6**, 2186 (2014).
29. Ramalingam, G., Perumal, N., Priya, A. K. & Rajendran, S. A review of graphene-based semiconductors for photocatalytic degradation of pollutants in wastewater. *Chemosphere* **300**, 134391 (2022).
30. Ivan, R. *et al.* Iron oxide/hydroxide–nitrogen doped graphene-like visible-light active photocatalytic layers for antibiotics removal from wastewater. *Sci. Rep.* **13**, 2740 (2023).
31. Zhan, M., Hong, Y., Fang, Z. & Qiu, D. Visible light-driven photocatalytic degradation of microcystin-LR by Bi_2WO_6/Reduced graphene oxide heterojunctions: Mechanistic insight DFT calculation and degradation pathways. *Chemosphere* **321**, 138105 (2023).
32. Zhang, L. *et al.* In situ crystallization and growth of TiO_2 nanospheres between MXene layers for improved adsorption and visible light photocatalysis. *Catal. Sci. Technol.* **11**, 3834–3844 (2021).
33. Allé, P. H., Fanou, G. D., Robert, D., Adouby, K. & Drogui, P. Photocatalytic degradation of rhodamine B dye with TiO_2 immobilized on SiC foam using full factorial design. *Appl. Water. Sci.* **10**, 207 (2020).
34. Di, G., Zhu, Zh., Zhang, H., Qiu, Y. & Yin, D. Simultaneous sulfamethazine oxidation and bromate reduction by Pd-mediated Z-scheme Bi_2MoO_6/g-C_3N_4 photocatalysts: Synergetic mechanism and degradative pathway. *Chem. Eng. J.* **401**, 126061 (2020).
35. Huanga, J. *et al.* Ultrathin Ag_2WO_4-coated P-doped g-C_3N_4 nanosheets with remarkable photocatalytic performance for indomethacin degradation. *J. Hazard. Mater.* **392**, 122355 (2020).
36. Qiao, Q. *et al.* Facile in situ construction of mediator-free direct Z-scheme g-C_3N_4/CeO_2 heterojunctions with highly efficient photocatalytic activity. *J. Phys. D: Appl. Phys.* **51**, 275302 (2018).
37. Hu, K. *et al.* Facile synthesis of Z-scheme composite of TiO_2 nanorod/g-C_3N_4 nanosheet efficient for photocatalytic degradation of ciprofloxacin. *J. Clean. Product.* **253**, 120055 (2022).
38. Xie, Z. *et al.* Construction of carbon dots modified MoO_3/g-C_3N_4 Z-scheme photocatalyst with enhanced visible-light photocatalytic activity for the degradation of tetracycline. *Appl. Catal. B: Environ.* **229**, 96–104 (2018).
39. Xu, H., Gan, Z., Zhou, W., Ding, Z. & Zhang, X. A metal-free 3C-SiC/gC_3N_4 composite with enhanced visible light photocatalytic activity. *RSC Advance.* **7**, 40028–40033 (2017).
40. Dong, H. *et al.* Theoretical investigations on SiC siligraphene as promising metal-free catalyst for oxygen reduction reaction. *J. Power Source.* **299**, 371–379 (2015).
41. Dong, H., Wang, L., Zhou, L., Hou, T. & Li, Y. Theoretical investigations on novel SiC_5 siligraphene as gas sensor for air pollutants. *Carbon* **113**, 114–121 (2017).
42. Gomi, L. S., Afsharpour, M., Ghasemzadeh, M. & Lianos, P. Bio-inspired N, S-doped siligraphenes as novel metal-free catalysts for removal of dyes in the dark. *J. Mol. Liquid.* **295**, 111657 (2019).
43. Afsharpour, M. & Amraee, A. R. Synthesis of bio-inspired N-doped SiC and investigation of its synergetic effects on Mo catalysts in oxidative desulfurization reaction. *Mol. Catal.* **436**, 285–293 (2017).
44. Gomi, L. S. & Afsharpour, M. Porous MoO_3@SiC hallow nanosphere composite as an efficient oxidative desulfurization catalyst. *Appl. Organometal. Chem.* **33**, e4830 (2019).
45. Afsharpour, M. & Khomad, E. Synthesis of bio-inspired porous silicon carbides using *Cortaderia selloana* and *Equisetum arvense* grasses as remarkable sulfur adsorbents. *Intern. J. Environ. Sci Technol.* **16**, 3125–3134 (2019).
46. Khomad, E. & Afsharpour, M. Green synthesis of nanostructured SiCs by using natural biopolymers (guar, tragacanth, Arabic, and xanthan gums) for oxidative desulfurization of model fuel. *Intern. J. Environ. Sci. Technol.* **16**, 2359–2372 (2019).
47. Gomi, L. S., Afsharpour, M. & Lianos, P. Porous SiO_2@SiC core-shell nanospheres functionalized with an amino hybrid of WO_3 as an oxidative desulfurization catalyst. *J. Indust. Eng. Chem.* **89**, 448–457 (2020).
48. Li, Y. *et al.* Efficient water disinfection with Ag_2WO_4-doped mesoporous g-C_3N_4 under visible light. *J. Hazard. Mater.* **338**, 33–46 (2017).
49. Liu, X. *et al.* The Three-Dimensional flower-like Bi_2WO_6 assisted by ethanolamine through a microwave method for efficient photocatalytic activity. *R. Soc. Open. Sci.* **6**, 181422 (2019).
50. Dkhilalli, F. *et al.* Characterizations and morphology of sodium tungstate particles. *R. Soc. Open. Sci* **5**, 172214 (2018).
51. Yang, D., Hernandez, J. A., Katiyar, R. S. & Fonseca, L. F. Surface Morphology-controlled fabrication of Na_2WO_4 films with high structural stability. *Chem. Phys. Lett.* **653**, 73–77 (2016).
52. De Santana, Y. V. B. *et al.* Silver molybdate and silver tungstate nanocomposites with enhanced photoluminescence. *Nanomater. Nanotechnol.* **4**, 22 (2014).
53. Li, X. *et al.* BiOBr with oxygen vacancies capture 0D black phosphorus quantum dots for high efficient photocatalytic ofloxacin degradation. *Appl. Surf. Sci.* **593**, 153422 (2022).
54. Wang, J., Zhang, Q., Deng, F., Luo, X. & Dionysiou, D. D. Rapid toxicity elimination of organic pollutants by the photocatalysis of environment-friendly and magnetically recoverable step-scheme $SnFe_2O_4/ZnFe_2O_4$ nano-heterojunctions. *Chem. Eng. J.* **379**, 122264 (2020).
55. Yeh, T. F., Cihlář, J., Chang, Ch. Y., Cheng, Ch. & Teng, H. Roles of graphene oxide in photocatalytic water splitting. *Mater. Today.* **16**, 78–84 (2013).
56. Hsu, L. C. *et al.* Adsorption of tetracycline on Fe (hydr)oxides: effects of pH and metal cation (Cu^{2+}, Zn^{2+} and Al^{3+}) addition in various molar ratios. *R. Soc. Open Sci.* **5**, 171941 (2018).
57. Mohammed, A. A., Al-Musawi, T. J., Kareem, S. L., Zarrabi, M. & Al-Ma'abreh, A. M. Simultaneous adsorption of tetracycline, amoxicillin, and ciprofloxacin by pistachio shell powder coated with zinc oxide nanoparticles. *Arab. J. Chem.* **13**, 4629–4643 (2020).
58. Hao, M., Fa, D., Qian, L. & Miao, Y. WO_3@ $Bi_2WO_6/NiWO_4$ nanocomposites with outstanding visible-light-driven photocatalysis for the degradation of organic dyes. *J. Nanosci. Nanotechnol.* **18**, 4788–4797 (2018).

59. Ghasemzadeh-mohammadi, V., Zamani, B., Afsharpour, M. & Mohammadi, A. Extraction of caffeine and catechins using microwave-assisted and ultrasonic extraction from green tea leaves: An optimization study by the IV-optimal design. *Food Sci. Biotech.* **26**, 1281–1290 (2017).
60. Ni, Z. *et al.* Facile construction of 3D hierarchical flower-like Ag_2WO_4/Bi_2WO_6 Z-scheme heterojunction photocatalyst with enhanced visible light photocatalytic activity. *Appl. Surf. Sci.* **576**, 151868 (2022).
61. Li, X. *et al.* Non-noble-metallic Ni_2P nanoparticles modified OV-BiOBr with boosting photoelectrochemical hydrogen evolution without sacrificial agent. *Appl. Catal. B: Environ.* **325**, 122341 (2023).
62. Wang, W. *et al.* Novel organic/inorganic PDI-Urea/BiOBr S-scheme heterojunction for improved photocatalytic antibiotic degradation and H_2O_2 production. *Chin. Chem. Let.* **33**, 5200 (2022).

Acknowledgements

Support of this investigation by Chemistry and Chemical Engineering Research Center of Iran is gratefully acknowledged.

Author contributions

The study conception design of study was done by M.A..Material preparation, data collection and analysis were performed by S.D.-F. and M.A.The manuscript was written by M.A..All authors read and approved the final manuscript.

Competing interests

The authors declare no competing interests.

Additional information

Supplementary Information The online version contains supplementary material available at https://doi.org/10.1038/s41598-023-37170-5.

Correspondence and requests for materials should be addressed to M.A.

Reprints and permissions information is available at www.nature.com/reprints.

Publisher's note Springer Nature remains neutral with regard to jurisdictional claims in published maps and institutional affiliations.